

A&A manuscript no.
(will be inserted by hand later)

Your thesaurus codes are:
9 (06.18.1; 06.06.3; 06.03.2; 02.16.1; 02.13.2)

ASTRONOMY
AND
ASTROPHYSICS

Solar flare radio pulsations as a signature of dynamic magnetic reconnection

B. Kliem¹, M. Karlický², and A.O. Benz³

¹ Astrophysical Institute Potsdam, An der Sternwarte 16, D-14482 Potsdam, Germany; bkliem@aip.de

² Astronomical Institute, Academy of Sciences, CS-251 65 Ondřejov, Czech Republic; karlicky@sunkl.asu.cas.cz

³ Institute of Astronomy, ETH, CH-8092 Zürich, Switzerland; benz@astro.phys.ethz.ch

Received 28 September 1999 / Accepted 29 May 2000

Abstract. Decimetric radio observations of the impulsive solar flare on October 5, 1992, 09:25 UT show a long series of quasi-periodic pulsations deeply modulating a continuum in the 0.6–2 GHz range that is slowly drifting toward lower frequencies. We propose a model in which the pulsations of the radio flux are caused by quasi-periodic particle acceleration episodes that result from a dynamic phase of magnetic reconnection in a large-scale current sheet. The reconnection is dominated by repeated formation and subsequent coalescence of magnetic islands (known as “secondary tearing” or “impulsive bursty” regime of reconnection), while a continuously growing plasmoid is fed by newly coalescing islands. Such a model, involving a current sheet and a growing plasmoid, is consistent with the Yohkoh observations of the same flare (Ohya & Shibata 1998). We present two-dimensional MHD simulations of dynamic magnetic reconnection that support the model. Within the framework of the proposed interpretation, the radio observations reveal details of plasmoid formation in flares.

Key words: Sun: radio radiation – Sun: flares – Sun: corona – Plasmas – MHD

1. Introduction

Although the physical origins of a number of solar radio burst types are well known, e.g., type II and type III bursts (Krüger 1979; Bastian et al. 1998), there are still many questions which types of the radio plasma emission emerge directly from the primary energy release of solar flares, which is supposed to result from magnetic reconnection in coronal current sheets (e.g., Priest 1982; Masuda et al. 1994; Tsuneta 1996). Furthermore, there are still different viewpoints regarding the question in which frequency range this radio emission can be observed.

Decimetric continuum radio bursts are often related to the impulsive phase of solar flares, and their frequencies correspond to the densities supposed to exist in the primary energy release volume. These bursts are usually

regarded to result from a distribution of flare-accelerated particles trapped in a coronal magnetic loop (Kuijpers 1980). In the trap, the particles develop a loss-cone distribution function, which is unstable and supports a plasma emission process that leads to fundamental emission near the electron plasma frequency, $\omega_{pe} = (4\pi ne^2/m_e)^{1/2}$, or to harmonic emission near $2\omega_{pe}$. According to this model, the bursts carry signatures not only of the particle acceleration in the primary energy release process, but also of the evolution of the trapped particle distribution in velocity space and of the evolution of the loop during the flare.

Continuum radio bursts, especially those in the decimetric wavelength range, often exhibit broad-band pulsations of the flux. The timescales lie typically in the range ~ 0.5 – 5 s. Proposed mechanisms of the pulsations fall into three categories: (1) MHD oscillations of a magnetic loop, which modulate the radio emissivity, (2) an oscillatory nonlinear regime of the kinetic plasma instabilities that emit the radio waves, and (3) a modulation of the acceleration of particles which represent the source of the wave energy (Aschwanden 1987). The third of these includes non-stationary magnetic reconnection.

Improved knowledge of magnetic reconnection in current sheets is imperative for resolving the flare problems. Such studies can be guided by radio observations, which often carry details of the dynamical plasma processes not visible at other wavelengths. In numerical simulations of reconnection (e.g., Ugai & Tsuda 1977; Sato & Hayashi 1979; Karlický 1988; Scholer 1991; Ugai 1992), as well as in the interpretation of soft X-ray observations (Tsuneta 1996), the focus has usually been on stationary Petschek-type reconnection. However, temporal fine structure is abundant in radio bursts and often also present in hard X-ray bursts (e.g., Kiplinger et al. 1983). Another problem lies in the fact that numerical simulations have to be performed in rather small boxes and over rather short time intervals. There is a permanent need to extend the simulations further in space (where they tend to reveal stronger dynamics) and in time, and attention must be

devoted to the re-scaling of the numerical results when specific observations are to be interpreted.

In the present paper we consider a pulsating decimetric continuum radio burst event. Its peak was coincident with the impulsive phase of a solar flare (October 5, 1992). Rather detailed knowledge of this flare is already available from a thorough analysis of its soft X-ray emission, which includes, in particular, the ejection of a plasmoid (Ohyama & Shibata 1998). We argue that the pulsations can be explained by modulations of particle acceleration in a highly dynamic regime of magnetic reconnection in an extended current sheet above the soft X-ray flare loop and that the radio emission process does not necessarily require trapping in a magnetic loop. The time profile of the radio burst appears to reflect the dynamics of the reconnection process directly. MHD simulations of reconnection in a long current sheet are presented to support the model. These simulations provide also further insight into the process of plasmoid formation in a current sheet, which is directly related to episodes of enhanced reconnection and enhanced particle acceleration.

The observations are presented in Sect. 2 and our MHD simulations are presented and scaled to coronal conditions in Sect. 3. A discussion of the new interpretation of pulsating continuum bursts and the conclusions are given in Sects. 4 and 5, respectively.

2. Observations

The flare on October 5, 1992, 9:25 UT was an impulsive, compact-loop, M2 class event that took place at the west limb, probably in active region NOAA 7293, which was located slightly behind the limb. Its hard X-ray lightcurve and the decimetric dynamic radio spectrum are plotted in Fig. 1 along with two characteristic single-frequency decimetric flux profiles. Fig. 2 shows the corresponding microwave burst.

The hard X-ray (HXR) emission showed a complex temporal evolution. The flare started with an extended period of low-level emission. The first impulsive rise near 9:24:25 UT was followed by several strong enhancements, each of $\gtrsim 10$ s duration (FWHM). The spectrum was hardest near 9:25:05 UT. The Yohkoh/HXT 14–23 keV and 23–33 keV band images (9:24:28–9:25:16 UT) show a single, slightly elongated source with centroid position just above the west limb (Sato et al. 1998). The weak microwave burst had a time profile similar to the HXR burst, but was much smoother. Also the GOES soft X-ray lightcurves (Solar Geophysical Data) show an impulsive rise near 9:24:25 UT, following a period of low-level activity.

The decimetric radio burst consisted of continuum emission superimposed with strong broadband pulsations during its whole lifetime. The general flux level varied in a complex manner during the event, showing several enhancements, as is typical of decimetric bursts. The

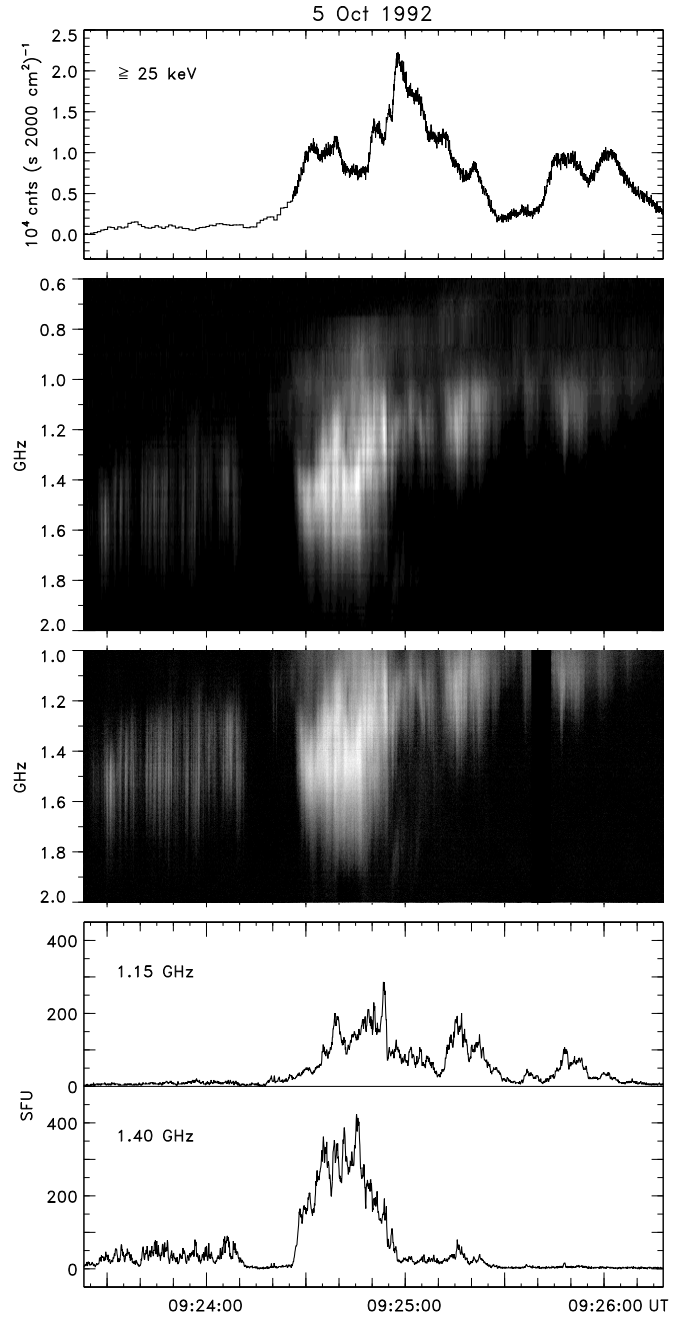


Fig. 1. The hard X-ray lightcurve of the October 5, 1992 flare (CGRO/BATSE/DISCSC data; top), the dynamic radio spectrum (Zürich and Ondřejov radiospectrographs; 2nd and 3rd panel, respectively), and two single-frequency cuts of the dynamic spectrum (bottom). The Ondřejov spectrum contains a gap of ≈ 6 s at 9:25:38 UT.

burst as a whole drifted towards lower frequencies at a rate ≈ -3 MHz s $^{-1}$. The main burst phase started at 9:24:27 UT at a frequency slightly higher than the preceding pulsations and with a temporarily much higher drift rate of ≈ -9 MHz s $^{-1}$. The average drift rate decreased

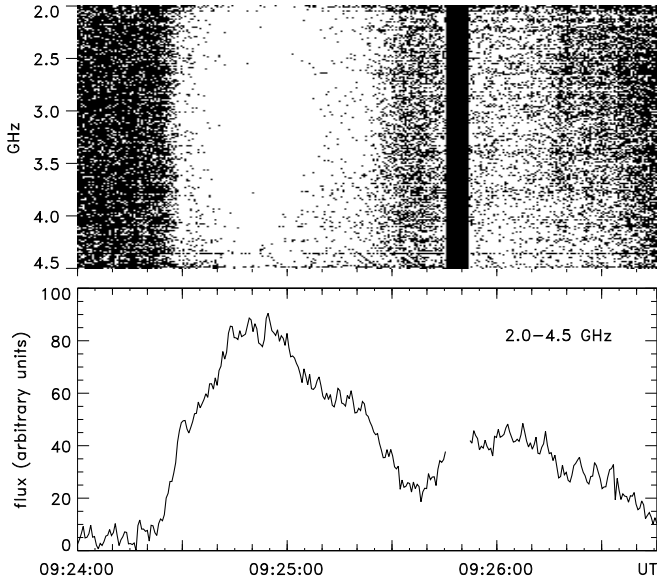


Fig. 2. High frequency radio continuum coincident with the rise of the hard and soft X-ray emissions (Ondřejov spectrograph).

toward the end of the event. The burst was weakly polarized, which is typical of type IV bursts from sources near the solar limb. It is not known whether the emission was fundamental or harmonic radiation. No other bursts were recorded at this time at frequencies below 0.6 GHz (Tremdsdorf and Zürich radiospectrographs).

Fig. 3 displays the pulsations during the early phase of the burst in greater detail. The intervals between the pulses and their individual durations were not regular, leading to a quasi-periodic appearance of the flux variations. The timescales of the pulses were lying in the range 0.5–3 s, and the FWHM of the auto-correlation was 1.3 s.

Two additional emission bands of low intensity existed during part of the burst (Fig. 4). The high-frequency band appeared only during a short interval (09:24:55–25:05 UT). Its drift and intensity variations were not correlated with the main band. The low-frequency band, which had an average frequency drift similar to the main band and weakly correlated intensity variations, could be discerned during \approx 09:24:20–09:25:25 UT. It is not clear whether it then decayed, or merged with the main band, or continued to drift but was masked by the low-frequency edge of the main band, which drifted to \sim 0.6 GHz at 09:26:18 UT.

The HXR lightcurve does not show much structure at short timescales (most of the fluctuations seen at the resolution of 64 ms in Fig. 1 are noise), but the auto-correlation (e.g. in the regular interval 09:23:28 to 09:24:13 UT) shows a FWHM of 4.5 s, indicating significant substructure in time. The 25–50 keV BATSE

lightcurve of the event considered here had been included in an earlier search for significant timescales in hard X-ray time profiles using a wavelet analysis method (Aschwanden et al. 1998), and a weak contribution around 4 s had been found in addition to the dominant timescale of \sim 28 s, which reflects the overlapping main pulses seen in Fig. 1.

HXR lightcurves are generally composed of a direct-precipitating component, which carries the information on the rapid variations of the acceleration process, and a smoothed component, leaking out of a trap, that has lost this information. A trap model could indeed be fitted to energy dependent time delays in the low-pass filtered HXR lightcurves of the considered flare (Aschwanden et al. 1997). This showed the importance of trapping in this flare and suggested a density in the trap of the HXR-emitting particles of order $n_{tr} \sim 10^{11} \text{ cm}^{-3}$, which is roughly in accordance with the density of the flare loop estimated from the soft X-ray data (see below).

There was a high correlation between the *general evolution* of the decimetric burst and the HXR lightcurve during the initial phase: the period of low-level emission and the impulsive onset of the main phase were coincident. The correlation became much weaker as the decimetric flux decreased in the course of the event. The strongest and hardest HXR peak was accompanied by only rather weak decimetric emission, but one of the main bunches of enhanced decimetric pulses later on (\approx 9:25:50 UT) was again nearly simultaneous with a significant HXR enhancement. The correlation of the general evolution shows that the decimetric burst was closely associated with the first impulsive energy release of the flare and with the processes that led to that energy release. Differences to the HXR burst in the later phases do not necessarily imply a loss of association, since the radio emission in general reflects not only the production of nonthermal particles but is also sensitive to changes in the magnetic field, which influence the slope of the particle distribution function and, hence, the growth rate of the plasma waves, and to density changes in the source and along the ray path, which influence the propagation of the radio waves. It is, however, quite probable that the strongest and hardest HXR peak resulted from flaring in a part of the active region that was not magnetically well connected with the decimetric source. The situation here is typical of comparisons between decimetric and HXR time profiles, where an association can often be established only from the coincidence of the main features like onset, main rise, or peak (Aschwanden et al. 1990).

A *detailed comparison* by cross-correlation was made for the initial, relatively regular part (shown in Fig. 3). The time resolution of the BATSE data in this pre-trigger interval is 1.024 s, so the correlation refers to structures of at least 2 s duration, which in general do not correspond to single decimetric pulses but to small groups. The cross-correlation coefficient has a distinct minimum

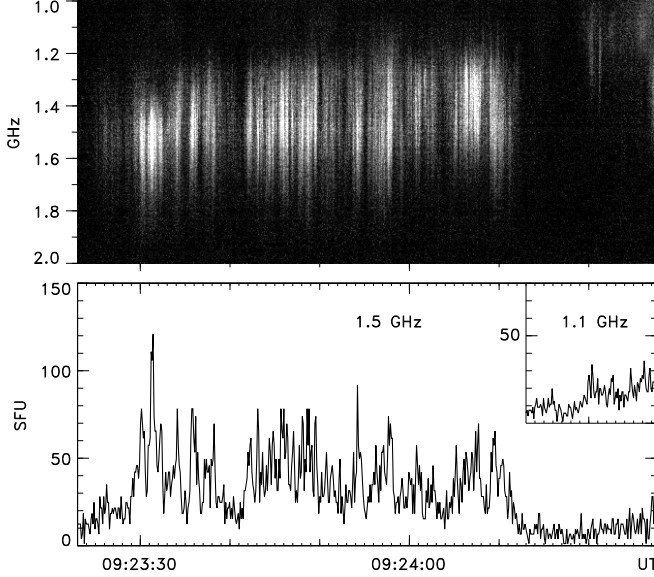


Fig. 3. Detail of the radio observations shown in Fig. 1 (Ondřejov spectrograph).

of -0.38 near zero lag, indicating a negative correlation (anti-correlation). Its FWHP of only 3.0 s suggests a trend for individual HXR pulses to peak when the radio flux reaches a minimum. The same property appears also in the main part of the event after subtracting a gliding-average background with 10 s or 20 s time constant.

The positive correlation of the general evolution of the decimetric and HXR lightcurves indicates the acceleration of the radiating electrons by the same global destabilization of the magnetic field configuration, and the anti-correlation of the details suggests acceleration by the same or by closely related spatial substructures — with a possibly complex relationship between the radio and HXR sources.

The soft X-ray images of the event, analysed by Ohyama & Shibata (1998), revealed a nearly stationary low-lying flare loop and a plasmoid ejection, which was first seen at $9:24:40$ UT at a height of $\approx 2 \times 10^4$ km. In addition, a large, faint loop was apparently connected with the rising plasmoid. The plasmoid was continuously accelerated and reached velocities of ≈ 250 km s $^{-1}$ at $9:25$ UT and ≈ 500 km s $^{-1}$ at $9:26$ UT. Temperatures and plasma densities in the soft X-ray structures were estimated by Ohyama & Shibata (1998) as follows: (a) in the flare loop at $9:24:18$ – $9:24:50$ UT: $T_{\text{fl}} = 7.1$ – 18 MK and $n_{\text{fl}} = (0.8$ – $6.7) \times 10^{10}$ cm $^{-3}$ and at $9:24:58$ – $9:25:58$ UT: $T_{\text{fl}} = 8.2$ – 20 MK and $n_{\text{fl}} = (1.4$ – $12) \times 10^{10}$ cm $^{-3}$; (b) in the plasmoid at $9:25:00$ UT: $T_{\text{pl}} = 10.6$ MK and $n_{\text{pl}} = (0.8$ – $1.6) \times 10^{10}$ cm $^{-3}$; and (c) in the expanding loop at $9:26:08$ UT: $n_{\text{el}} = (3.2$ – $9.4) \times 10^9$ cm $^{-3}$ under the

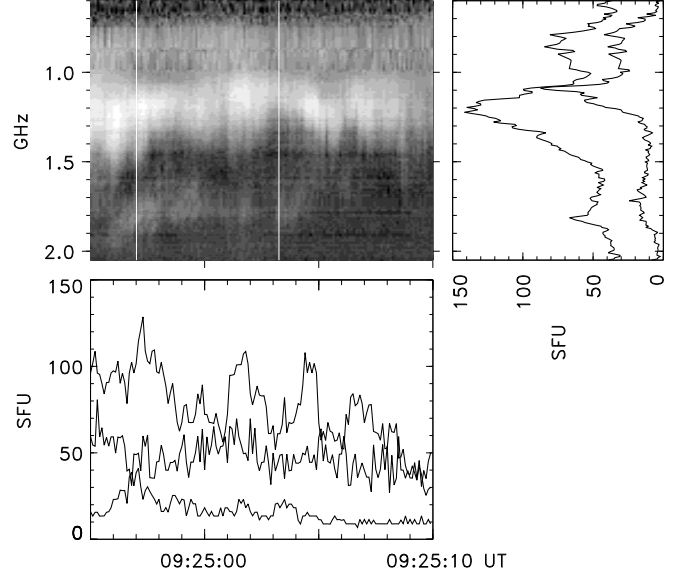


Fig. 4. Detail of the three-band structure during part of the burst shown in Fig. 1 (Zürich spectrograph). Time profiles in the bottom panel are taken at 1.16 , 0.90 , and 1.8 GHz (in order of decreasing flux). The times of the instantaneous spectra (top right) are indicated by the white lines in the dynamic spectrum. The spectrum at $9:24:57$ UT is shifted by 30 SFU for clarity.

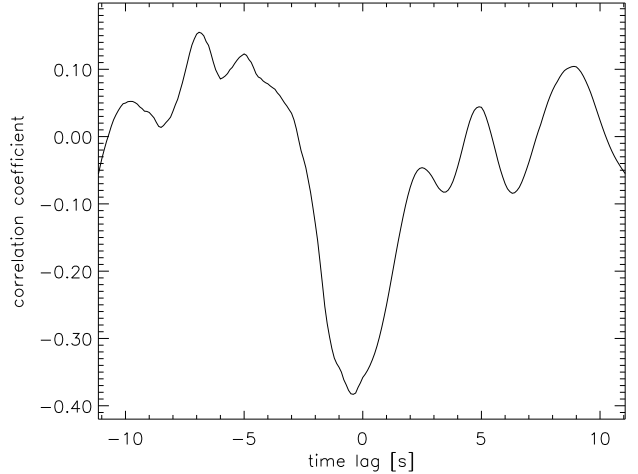


Fig. 5. Cross correlation of the BATSE hard X-ray flux (≥ 25 keV) and the decimetric flux integrated between 0.6 and 2 GHz in the interval $09:23:28$ – $09:24:13$ UT.

assumption of $T_{\text{el}} = 2$ MK and $n_{\text{el}} \sim (1.2$ – $4) \times 10^9$ cm $^{-3}$ for T_{el} in the range 4 – 14 MK.

Parameters in the current sheet, supposed to exist between the nearly stationary flare loop and the rising plasmoid, were not explicitly given but can be es-

timated from Fig. 7 of Ohyama & Shibata (1998) as $n_{\text{CS}} \sim 10^{10} \text{ cm}^{-3}$ and $T_{\text{CS}} = 9 \times 10^6 \text{ K}$ at 9:25:18 UT. (The latter values may actually refer to the rear side of the plasmoid, which formed an elongated structure.) In comparison, the most intense radio emission in the 1.1–1.6 GHz frequency range implies source densities in the range $n = (1.5\text{--}3.2) \times 10^{10} \text{ cm}^{-3}$ in case of fundamental or $n = (0.4\text{--}0.8) \times 10^{10} \text{ cm}^{-3}$ in case of harmonic radiation. Although the uncertainties are substantial, it is apparent that the densities in the radio source correspond more closely to the densities in the plasmoid and in the current sheet than to the densities in the flare loop or in the expanding loop (for the reasonable assumption of $T_{\text{el}} \gtrsim 4 \text{ MK}$). The substantial increase of the density in the flare loop during the event rules this loop out as site of the radio source, since the radio emission showed, on average, a negative frequency drift.

3. A model based on dynamic reconnection

Interpretations of the pulsations in the considered event in terms of existing models for the modulation of a magnetic loop by MHD waves can be ruled out, because these models predict pulsations with regular or slowly varying period and most of them also with constant or exponentially decaying amplitude (see Aschwanden 1987), while the observed intervals between the pulses, the durations, and the peak intensities were all varying rapidly and partly irregularly.

The geometry of this *eruptive* flare and the observed relation between HXR and decimetric radio pulsations are not suggestive of modulations by oscillatory nonlinear instabilities of electrons stably trapped for more than a minute. It appears more obvious to relate the pulsations to changes of the plasma environment and to the corresponding modulations of the particle acceleration or radio emissivity than to oscillatory nonlinear kinetic processes in an idealized stationary trap or current sheet model.

The Yohkoh observations provide strong evidence that a current sheet lying above the soft X-ray flare loop and an outward propagating plasmoid were essential elements of the flare under consideration. The basic magnetic topology appears to be similar to the 2D Kopp-Pneuman model of flares (see, e.g., Tsuneta 1996). Estimates of the energy content of the plasmoid suggested that it did not contain sufficient energy to form the current sheet by sweeping up an overlying closed magnetic field structure (Ohya & Shibata 1998). Thus, either the plasmoid was formed and accelerated by processes operating in the preexisting current sheet, or it was formed jointly with the current sheet by a global MHD instability.

Considering the limited frequency extent and average frequency drift of the observed radio burst, and the estimated densities, we interpret the burst as emission originating from the plasmoid (or from dense plasmoid-like structures in the current sheet). The frequency drift of

the burst can then be attributed to the ejection of the plasmoid (or to the corresponding upward expansion of the current sheet).

To explain the radio pulsations, we focus on small-scale MHD processes within the current sheet, disregarding aspects of interaction with the dense flare loop lying below the current sheet. We expect that the small-scale dynamics in the current sheet will be similar in the two variants of plasmoid formation, which were mentioned above, since the magnetic topology and the large-scale plasma flows become similar, once a plasmoid is formed. Here we will concentrate on the former case, i.e., spontaneous reconnection triggered by an initial perturbation within the current sheet; no driving flows are prescribed at the boundaries of the numerical system. We note that such flows could not be specified from the existing observations of the event.

A two-dimensional (2D) model appears to be well justified to study effects intrinsic to the current sheet, since the size of the plasmoid along the line of sight was estimated to be of order 10^4 km , which exceeds the supposed current sheet width by several orders of magnitude. Although the expanding loop-shaped structure, if it was really connected with the plasmoid, implies the presence of a magnetic guide field component, we restrict ourselves here further to the case of vanishing guide field, i.e., an initially antiparallel (“neutral”) current sheet is studied. As long as the internal current sheet dynamics including the formation and acceleration of the plasmoid are concerned, this simplification also appears reasonable within the 2D approximation for the following reason. In 2D incompressible MHD, an initially homogeneous guide field is only passively advected, it has no influence on the dynamics. In 2D simulations of compressible current sheet dynamics, its influence has been found to remain very small (Ugai 1993). (A guide field becomes essential in 3D reconnection studies, where it can lead to the formation of structures like interlinked flux tubes, which are otherwise absent.)

Magnetic reconnection is often considered in the framework of the stationary Petschek model (e.g., Ugai 1992, 1995; Yokoyama & Shibata 1994; Tsuneta 1996) and its generalizations (Priest & Forbes 1986). However, there is a long-lasting dispute whether stationary Petschek reconnection is possible (Biskamp 1986; Forbes & Priest 1987; Scholer 1991; Kulsrud 1998). For long current sheets, numerical simulations indicated that resistive magnetic reconnection proceeds in a time-variable manner, involving repeated formation of magnetic islands and their subsequent coalescence (Biskamp 1982, 1994; Scholer & Roth 1987; Karpen et al. 1995). This is particularly true if the resistivity is permitted to vary. The process is known as “secondary tearing” or as the “impulsive bursty” regime of reconnection (Priest 1985). The repeated coalescence of islands may lead to the formation of a growing, and eventually large-scale, plasmoid (Scholer & Roth 1987; Schumacher & Kliem 1996; Magara et al. 1997). Coincident with the formation of each new magnetic island, the

electric field at the new magnetic X point is enhanced. This probably leads to a burst of accelerated particles (although the detailed mechanisms of particle acceleration in reconnection regions still remain unknown). In the simplest model, each formation of a new magnetic X point corresponds to a burst of acceleration, which, in its turn, corresponds to an enhancement of the radio flux (one pulsation). More complicated schemes are conceivable and briefly discussed in Sect. 4.

3.1. Basic equations and simulation method

The equations of compressible, resistive one-fluid MHD used in this paper are

$$\partial_t \rho = -\nabla \cdot (\rho \mathbf{u}), \quad (1)$$

$$\rho \partial_t \mathbf{u} = -\rho (\mathbf{u} \cdot \nabla) \mathbf{u} - \nabla p + \mathbf{j} \times \mathbf{B}, \quad (2)$$

$$\partial_t \mathbf{B} = \nabla \times (\mathbf{u} \times \mathbf{B}) - \nabla \times (\eta \mathbf{j}), \quad (3)$$

$$\partial_t U = -\nabla \cdot \mathbf{S}, \quad (4)$$

where the current density \mathbf{j} , the total energy density U , and the flux vector \mathbf{S} are given by

$$\mathbf{j} = \frac{1}{\mu_0} \nabla \times \mathbf{B},$$

$$U = \rho w + \frac{\rho}{2} u^2 + \frac{B^2}{2\mu_0},$$

$$\mathbf{S} = (U + p + \frac{B^2}{2\mu_0}) \mathbf{u} - (\mathbf{u} \cdot \mathbf{B}) \frac{\mathbf{B}}{\mu_0} + \eta \mathbf{j} \times \frac{\mathbf{B}}{\mu_0},$$

and w is the internal energy per unit mass, which is related to the pressure through the equation of state, $p = (\gamma - 1) \rho w$. In the two-dimensional model adopted here, $\partial/\partial z = 0$ for all quantities and $B_z = u_z = 0$; hence the current density and the electric field possess only z components. Further, the ratio of specific heats is $\gamma = (N + 2)/N = 2$, where N is the number of degrees of freedom. The electric field is given by

$$\mathbf{E} = -\mathbf{u} \times \mathbf{B} + \eta \mathbf{j}. \quad (5)$$

An antiparallel Harris equilibrium (a neutral current sheet) with uniform density is chosen as the initial condition:

$$\mathbf{B} = -B_0 \tanh(y/l_{CS}) \mathbf{e}_x, \quad (6)$$

$$\mathbf{u} = 0, \quad (7)$$

$$\rho = \rho_0, \quad (8)$$

$$p = (1 + \beta) B_0^2 / (2\mu_0) - B_x^2 / (2\mu_0), \quad (9)$$

where the plasma beta is defined as $\beta = 2\mu_0 p(|y| \rightarrow \infty) / B_0^2$.

The variables are normalized by quantities derived from the current sheet half width l_{CS} and the asymptotic ($|y| \rightarrow \infty$) Alfvén velocity $V_A = B_0 / (\mu_0 \rho_0)^{1/2}$ of the configuration at $t = 0$. Time is measured in units of the Alfvén time $\tau_A = l_{CS} / V_A$, and p , \mathbf{E} , \mathbf{j} , and η are normalized by

$B_0^2 / (2\mu_0)$, $V_A B_0$, $B_0 / (\mu_0 l_{CS})$, and $\mu_0 l_{CS} V_A$, respectively. Then the Lundquist number is given by $S = \eta^{-1}$. The normalized variables will be used in the remaining part of this subsection.

The equilibrium is initially perturbed by a localized resistivity

$$\eta(x, y, t \leq t_0) = 0.02 \exp[-(x/0.8)^2 - (y/0.8)^2], \quad (10)$$

fixed for a few Alfvén times, $t_0 = 10$. Thereafter the resistivity is variable and is determined self-consistently at every grid point and time step from the electron-ion drift velocity $v_D = v_0 j / \rho$ (where the factor $v_0 = v_D(0) = d_i / l_{CS}$ results from the normalization and $d_i = c / \omega_{pi}$ is the ion inertial length). An “anomalous” value, η_{an} , is set if a threshold, v_{cr} , is exceeded, otherwise vanishing resistivity is assumed:

$$\eta(\mathbf{x}, t) = \begin{cases} 0 & : |v_D| \leq v_{cr} \\ C \frac{(|v_D(\mathbf{x}, t)| - v_{cr})}{v_0} & : |v_D| > v_{cr}. \end{cases} \quad (11)$$

Here $C = 0.003$ and $v_{cr} = 3v_0$. Such a resistivity model is customary in MHD simulations of magnetic reconnection (e.g., Ugai 1992; Yokoyama & Shibata 1994). We have verified that the dynamics of the system does not significantly depend on the particular choice of the parameters t_0 , C , and v_{cr} in a substantial range around the values used here. Also the dependence on β is weak. Simulations with $\beta > 1$ show less variable secondary tearing. We present a low-beta simulation, $\beta = 0.15$.

Eqs. (1)-(4) are transformed into a flux conserving form, $\partial_t \Psi + \partial_x \mathbf{F}(\Psi) + \partial_y \mathbf{G}(\Psi) = 0$, for each of the six integration variables, $\Psi = (\rho, \rho u_x, \rho u_y, B_x, B_y, U)$, where \mathbf{F} and \mathbf{G} are the nonlinear flux terms. A two-step Lax-Wendroff scheme according to Ugai & Tsuda (1977) and a uniform Cartesian grid with resolutions $\Delta x = \Delta y = 0.045$ are employed for the numerical integration. In order to stabilize the scheme, artificial smoothing (Sato & Hayashi 1979) is applied such that the variables at each grid point are replaced after each full time step of the Lax-Wendroff algorithm in the following manner

$$\Psi_{ij}^n \longrightarrow \lambda \Psi_{ij}^n + \frac{1-\lambda}{4} (\Psi_{i+1,j}^n + \Psi_{i-1,j}^n + \Psi_{i,j+1}^n + \Psi_{i,j-1}^n)$$

with λ varying in the range 0.97–0.98 during the simulation.

In order to study the effect of secondary tearing, the numerical box must not be too small. For box lengths $L_x \sim 20$, which is a common value in the literature, secondary tearing occurs only for rather small box heights, $L_y \sim 4$. Increasing the box length to $L_x \sim 40$, leads to secondary tearing for all reasonable values of L_y , however, the details of the time profile of the reconnection rate, in particular the development of irregular or quasi-periodic reconnection, depend on L_x until L_x exceeds a value ~ 60 . The simulation presented here used $L_x = 64$ and $L_y = 16$.

The simulation is carried out in the first quadrant, using symmetrical boundary conditions at the lower and left boundaries. Open boundary conditions are realized at $\{x = L_x\}$ and $\{y = L_y\}$ by the requirement that the normal derivatives of all variables vanish, except for the normal component of \mathbf{B} , which is determined from the solenoidal condition.

3.2. Dynamic magnetic reconnection

The dynamical evolution of the considered system, shown in Figs. 6 and 7, starts as in many other investigations of spontaneous reconnection (e.g., Ugai 1992). The initial perturbation causes a small burst of reconnection at the origin, which leads to acceleration of plasma along the x axis by the Lorentz force $f_x = -jB_y$. Mass conservation then enforces an inflow u_y into the region of the initial perturbation. This convects new magnetic flux toward the sheet and causes the current density to increase again locally. After $\sim 70 \tau_A$, the threshold v_{cr} is exceeded and anomalous resistivity is spontaneously excited at the origin. This enables a positive feedback between reconnection, acceleration of the fluid, and the local rise of the resistivity. The continuing and initially amplifying reconnection leads to a strong outflow of heated plasma along the x axis, which eventually reaches the Alfvén velocity and drives a high-pressure region in front of it toward the outer boundary. The state of the system during this phase of amplifying Petschek-like reconnection is illustrated in Figs. 6 and 7 at $t = 80$ and $t = 158$, where the current density ridges near the separatrix lines of the magnetic field delineate the slow mode shocks.

Since the level of anomalous resistivity at the origin can adjust to changes in the outer region, it has often been assumed that a balance between convection and diffusion is reached and that, consequently, the Petschek-like reconnection state, once formed, does approach stationarity (e.g., Ugai 1992). Also many observational studies of solar eruptions have assumed that stationary Petschek reconnection occurred (e.g., Tsuneta 1996). However, stationary Petschek reconnection has been obtained in numerical experiments only if a localized resistivity was held fixed in time or if the box length was small, $L_x \lesssim 20$ (see Scholer 1991). Variable resistivity leads to non-stationary reconnection if the current sheet is sufficiently extended, independent of whether the resistivity model is based on the electron-ion drift velocity or on the current density (Scholer & Roth 1987). This has recently been confirmed for 3D reconnection as well (Schumacher et al. 2000).

The principal effect that leads to variable reconnection appears to be the inability of the fluid to carry a sufficient amount of magnetic flux into the strongly localized diffusion region to support the Alfvénic outflow of reconnected flux in steady state (Kulsrud 1998). The free acceleration of the plasma, which is penetrated by reconnected field lines, into the x direction causes the inflow to steepen the

current density around the origin in a range of increasing extent. Although, according to Eq. (11), the density depression at the origin tends to keep the anomalous resistivity more localized than the range of enhanced current density, also the area of anomalous resistivity excitation increases into the x direction. Its extent reaches $\delta x_\eta = 13$ at $t = 200$. At the same time, the width of the anomalous resistivity region in the y direction stays approximately constant, $\delta y_\eta \approx 0.2$. The central part of the current sheet has thus formed a Sweet-Parker configuration, which implies a reduction of the reconnection rate in comparison to the Petschek configuration ($t \approx 100$ – 200). The acceleration of the fluid is then also reduced locally, and both the current density peak and the density depression at the origin are reduced. A resistivity maximum remains at the edge of the elongated η_{an} area, while the resistivity drops to zero between the new maximum and the origin. This leads immediately to the formation of a new X point (and its mirror image) at $t \approx 200$ — the so-called secondary tearing (Scholer & Roth 1987).

The sequence then repeats at the new X point, where the level of the resistivity and the field line reconnection are initially also strongly amplified. This drives the coalescence of the magnetic islands between the three X points, resulting in a plasmoid at the origin. Over the next ~ 200 Alfvén times, the magnetic structure at the new X point becomes flat and the resistivity area elongates and splits again, forming a new X point further out ($t \approx 400$). The corresponding magnetic island is again driven toward the central plasmoid by the rapidly evolving new X point. Over a period of $1200 \tau_A$, seven strong new X points are created, supplemented by a number of weak X and O pairs which can be considered as “fluctuations” and are of little dynamical importance. All seven magnetic islands merge with the central plasmoid, while some of the “fluctuations” merge with the outflow. This merging is accompanied by transient excitations of anomalous resistivity between the approaching islands (see Fig. 6 at $t = 479$).

An integral view of the dynamics is given in Fig. 8, where the electric field at the various main X points (i.e., the reconnection rate) and the location of the dominant X point in the system are plotted. The seven new main X points are separated using different linestyles. Their individual variations contain imprints of the additional formations of weak X points, which disturb the magnetic configuration and the outflow from the main X points. The “dominant” X point in the bottom panel is the one where instantaneously the highest reconnection rate occurs. The change-over of maximum reconnection to a stronger new X point further out marks jumps in the position of the dominant X point. It is apparent from the figure that the secondary tearing leads to higher reconnection rates than the Petschek-like reconnection, which exists only during the first $\sim 200 \tau_A$. The reconnection rate in the numerical experiment is of the same order as that implied by the observations, $R_{obs} \sim 0.02$ (Ohya & Shibata 1998). The

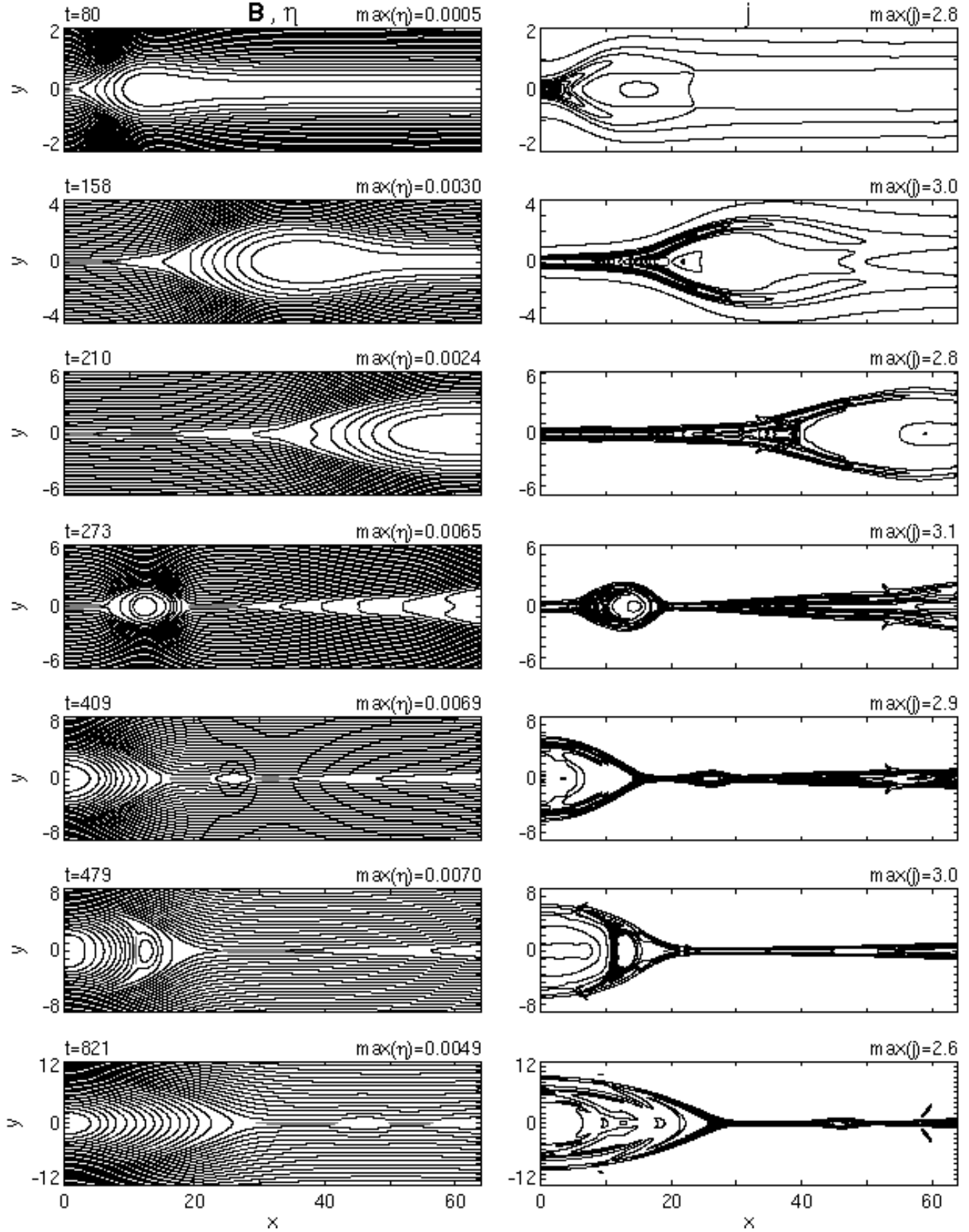


Fig. 6. Magnetic field (left panels) and current density (right panels) at characteristic times of the evolution. The regions, where anomalous resistivity is excited, are shown shaded in the magnetic field plots.

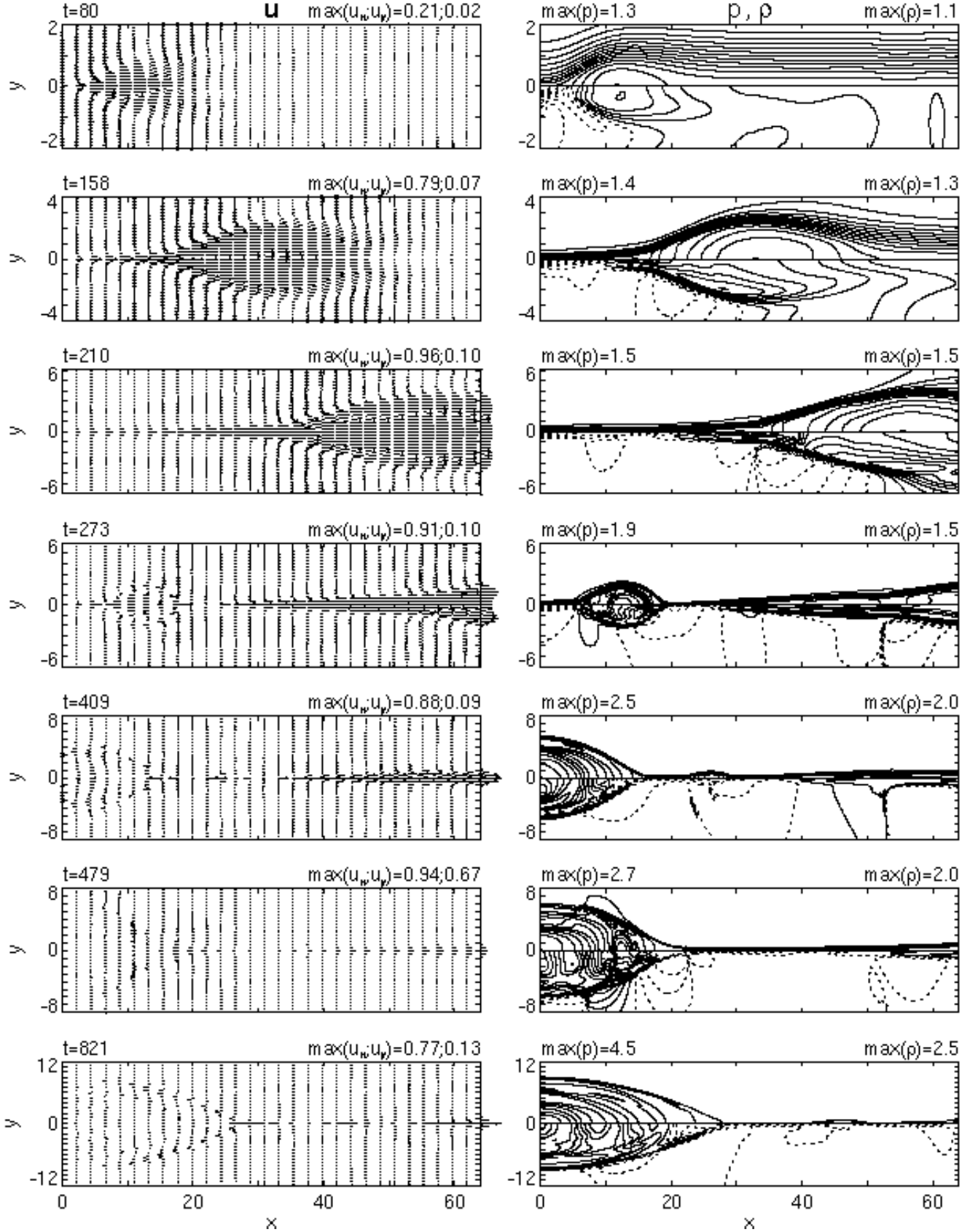


Fig. 7. Velocity field (left panels), pressure (right panels, $y > 0$), and density (right panels, $y < 0$) at the same times as in Fig. 6. Contours of rarefactions ($\rho < 1$) are shown dashed.

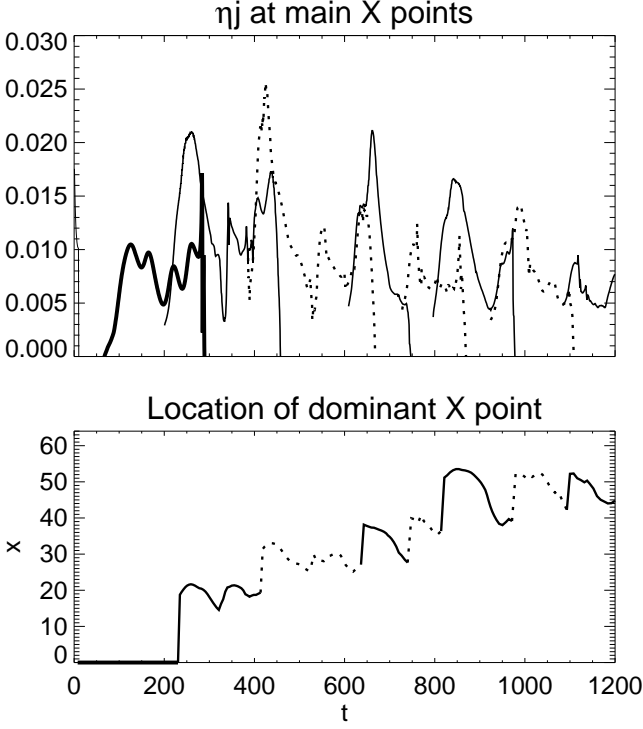


Fig. 8. Top: Electric field at the main X points (reconnection rate) vs. time. Thick line: Petschek-like reconnection with a central X point ($t \approx 70-200$) and forced reconnection by initial island coalescence at the origin ($t \approx 200-300$). Medium line width (solid and dotted): main new X points. Thin line: initial perturbation. Bottom: Location of the dominant X point.

intervals between the reconnection peaks are not uniform, but also not completely irregular.

As a result of secondary tearing, the central plasmoid is continuously fed with heated material carrying reconnected magnetic flux. The highly variable inflow into the plasmoid from the neighbouring X points triggers oscillations of the plasmoid as a whole. These oscillations in their turn enhance the time variability of the highly non-linear, threshold-depending reconnection process in the outer parts of the extended current sheet. The pressure and density in the plasmoid are continuously rising, causing it to expand in the x and y directions. This expansion appears to be the reason of the general slow decline of the activity seen in Fig. 8 after $t \approx 400$. The increasing width of the plasmoid in the y direction makes the convection of new magnetic flux toward the neighbouring X point more difficult because an increasing amount of field line bending is required, and the space available to form an extended flat current sheet section between the plasmoid and the boundary L_x is reduced. This decrease of the average reconnection rate is expected to be far smaller in the solar corona, where the magnetic islands are much more

elongated in the x direction and less field line bending is required (see Sect. 3.4).

We have seen that the dynamical evolution leads to two types of dense structures. The first one is the symmetric pair of high-pressure regions driven ahead of the outflow, which commences with the initial perturbation. This structure is commonly referred to as plasmoid, although only the field lines at its rear side are closed, while the field lines at its front side close at infinity. (In the numerical experiment, a small fraction of the flux closes also at its front side, due to the nonvanishing numerical diffusion.) The second one is the plasmoid resulting from secondary tearing. Fig. 9 shows that pressure and density in both plasmoids rise with time to values far in excess of the initial ones and that the rise is much stronger in the central plasmoid. For both plasmoids one can see that the density ratio $r_n = \rho_{pl}/\rho_0$ remains much smaller than the corresponding pressure ratio. This is due to the strong plasma heating in the dissipation region around the X points. In the solar corona one can expect that the size ratio of dissipation region and plasmoid is far smaller than in the simulation and that the pressure enhancement is to a larger fraction realized as a density enhancement. The soft X-ray images of the plasmoid in the considered flare suggest a density ratio to the surrounding corona of ~ 10 (Ohyama & Shibata 1998). Keeping in mind that the overall scales of the numerical experiment, $L_x = 64$ and $t_{\max} = 1200$, are by orders of magnitude smaller than those of the flare, the formation of a plasmoid with a density enhancement $r_n \sim 10$ in the flare by the secondary tearing and subsequent coalescence processes appears to be possible.

The central plasmoid cannot move in the symmetrical simulation. In a small range of parameter values, it can tear and leave the box in two parts (Kliem & Schumacher 1996). If the condition of symmetry about the y axis is relaxed, small asymmetries build up, which eventually lead to strong acceleration of the plasmoid. Previous simulations showed that a plasmoid can be formed also in the presence of asymmetries if their initial value is small (Schumacher & Kliem 1996). There it was further found that the pressure and density in the plasmoid continue to rise during the acceleration and ejection of the plasmoid and that the velocity of the plasmoid can reach a significant fraction of the Alfvén velocity ($\sim 0.3 V_A$).

As long as the plasmoid is being formed at a fixed position, its density is increasing. Only if the plasmoid starts to move along the current sheet to greater heights, it will expand and its pressure and density will decrease again according to the decreasing pressure of the surrounding medium. The density ratio to the surrounding material may stay constant, or may even increase further, as long as the reconnection continues.

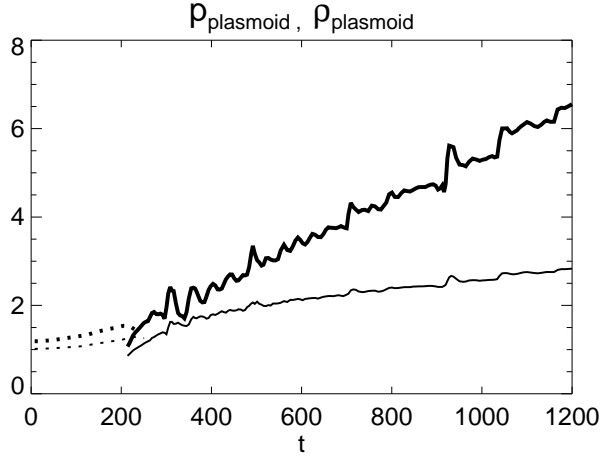


Fig. 9. Peak pressure (thick lines) and density (thin lines) of the plasmoid formed by the initial perturbation (dotted) and of the central plasmoid formed by secondary tearing. The initial normalized values are $p_0(y=0) = 1 + \beta = 1.15$ and $\rho_0 = 1$.

3.3. Particle acceleration, trapping, and radio emission

It is well known that particles are accelerated near the X points in the DC electric field associated with magnetic reconnection (e.g., Deeg et al. 1991; Moses et al. 1993; Birn et al. 1998). A multiple X point reconnection process, characteristic of secondary tearing and other forms of impulsive bursty reconnection (like the multiple coalescence instability), strongly enhances the number of accelerated particles and their maximum energy in comparison to single X point reconnection, where the particles can quickly escape (Ambrosiano et al. 1988; Scholer & Jamitzky 1987; Kliem 1994; Kliem et al. 1998). Peaks of the reconnection rate, such as seen in Fig. 8, represent temporal peaks of the electric field at the X points and, hence, correspond to peaks of particle acceleration by the DC electric field. The same is true for models of stochastic particle acceleration which suppose that the primary MHD wave spectrum is excited by the reconnection process (Miller et al. 1996). Although the physics of particle acceleration in reconnection regions still appears to be far from being understood, the existing investigations strongly suggest that a significant fraction of the particles in a dynamic current sheet can be accelerated to near-relativistic and relativistic energies. An investigation of particle acceleration in a current sheet that undergoes secondary tearing is planned for a future study.

The strongest electric fields occur at the main magnetic X points adjacent to the plasmoid and, thus, a large fraction of the accelerated particles becomes trapped in the plasmoid. The other part can escape along the field lines of the reconnection outflow. Those particles escaping with the downward directed outflow are likely to become

trapped in the magnetic cusp configuration between the current sheet and the underlying flare loop. Such trapping may explain the dominance of the trap-leakage component in the hard X-ray lightcurve and contribute to the decrease of the correlation between the general evolution of the hard X-ray and decimetric flux profiles in the course of the event (i.e., with increasing plasmoid height).

In a strictly two-dimensional configuration, the particles in the central plasmoid are trapped indefinitely (e.g., Scholer & Jamitzky 1987). In reality, also this part can escape from the plasmoid along the z direction, either by (slow) guiding centre drifts into the z direction, or by free streaming if a guide field $B_z \neq 0$ exists.

It is not clear whether the dynamic current sheet that forms a plasmoid does also form a loop-shaped magnetic trap (which is the canonical source model of several radio burst types, including decimetric continuum bursts). A highly distorted magnetic loop, or flux rope, may be associated with the central plasmoid if a significant guide field component ($B_z > B_{x0}$) is present. Such a configuration was, in fact, suggested for the considered flare by Ohya & Shibata (1998). However, due to the magnetic shear introduced by a $B_z \neq 0$ in the vicinity of the plasmoid, the photospheric footpoints of the field lines that are connected to the plasmoid may be widely dispersed in this case, and it is not clear whether a loss-cone distribution function can be formed. Therefore, it is possible that an alternative source model is required for the radio burst. Since the accelerated particles may gain excess perpendicular energy from drifts in the inhomogeneous magnetic field near the X points (Kliem 1994), they may be immediately unstable (i.e., within the current sheet and the plasmoid) to excitation of upper hybrid waves, which easily transform into radio emission, and the presence of a magnetic trap may not be necessary to form a radio source.

3.4. Scales in coronal current sheets

In this section we investigate how the scales found in the numerical experiment transform for parameters of the middle solar corona, where soft X-ray ejecta and decimetric radio sources are generally formed. As characteristic plasma parameters in the centre of the current sheet, we take the values that can be inferred for the flare of October 5, 1992 from Figs. 6 and 7 in Ohya & Shibata (1998), i.e., $n_{CS} \sim 10^{10} \text{ cm}^{-3}$ and $T_{CS} = 9 \times 10^6 \text{ K}$ (Sect. 2). These values refer to a dense and heated (i.e., presumably active) current sheet or possibly to the trailing part of the extended plasmoid, which had not yet reached a great height by the time of these parameter determinations (9:25:00–9:25:18 UT). The plasma surrounding the current sheet was much less dense and much less hot, as was the current sheet itself in the Yohkoh/SXT images at a later stage of the evolution. A typical value of the coronal background plasma density at the considered heights

($h \sim 2 \times 10^9$ cm) is $n_0 \sim 10^9$ cm $^{-3}$. As coronal background temperature we will take $T_0 \sim 2.5 \times 10^6$ K. The maximum instantaneous bandwidth of the decimetric radio burst suggests that the density varied by a factor ≈ 4 within the radio source.

Although the plasma parameters estimated by Ohyama & Shibata are subject to uncertainties that derive from necessary assumptions on the scale of the structures along the line of sight ($L_z = 10^9$ cm) and the filling factor ($f = 1$), they are consistent with the parameters derived for another flare which showed a plasma ejection (Tsuneta 1997). We note that a density of $\sim 10^{10}$ cm $^{-3}$ at the electron acceleration site was found also for other flares, using a different method (by determining the starting frequency of forward and reversely drifting type III burst pairs; see Aschwanden et al. 1993).

Estimates of the magnetic field strength B_0 in the plasma surrounding the current sheet are also rather uncertain. Ohyama & Shibata (1998) obtained $B_0 \sim 70$ G from the condition of pressure equilibrium across the current sheet, $B_0^2/8\pi = P_{CS} - P_0$, using a rough estimate of the internal and external pressures, P_{CS} and P_0 , respectively (actually they supposed a higher pressure than implied by the values of n_{CS} and T_{CS} given above). This way of estimating B_0 is rather sensitive to the filling factor of the high-pressure current sheet plasma in the area of one detector pixel, $B_0 \propto f^{-1/2}$ for $P_{CS} \gg P_0$. Hence, a smaller as well as a higher value of the magnetic field would also be plausible. Nevertheless, we shall use $B_0 \sim 70$ G, which gave a reasonable estimate of the flare energy balance. Using this with n_0 and T_0 , the Alfvén velocity and the plasma beta outside of the current sheet become $V_A \sim 4.8 \times 10^8$ cm s $^{-1}$ and $\beta \sim 3.5 \times 10^{-3}$, respectively.

The current sheet half width can be estimated from the threshold condition for onset of kinetic current-driven plasma instabilities. Spontaneous excitation and re-excitation of anomalous resistivity implies that the ion-electron drift velocity in the sheet remains close to the critical value v_{cr} . This critical drift velocity is of the order of the ion thermal velocity, $v_{ti} = (T_i/m_i)^{1/2}$, for the three most relevant instabilities and a wide range of parameter values. The three most relevant instabilities are the lower-hybrid-drift instability, the electrostatic ion cyclotron instability, and the ion sound instability (see, e.g., the review by Papadopoulos 1979). Using $v_{cr} = v_{ti}$, Ampère's law yields $l_{CS} \sim 4\beta^{-1}r_{ci}$, where $r_{ci} = v_{ti}/\omega_{ci}$ is the ion cyclotron radius. For our external values n_0 and T_0 we find $l_{CS} \sim 2 \times 10^4$ cm. The corresponding Alfvén time is only 5×10^{-5} s.

When considering the direction along the magnetic field, we have to recall that a fluid model is valid only on scales L larger than the mean free path, $L > \lambda_{mfp}$. In the fluid model, this length is the lower limit of inhomogeneity scales of η , which set the distance δ_x between neighbouring X points. Since the formation of inhomogeneities in

the current sheet is permanently enforced by the outflow along the x axis of material that carries reconnected field lines, it appears reasonable to suppose that $\delta_x \sim \lambda_{mfp}$. The mean free path is of order 5×10^7 cm for both pairs of density and temperature values (n_0, T_0) and (n_{CS}, T_{CS}) [but varies by a factor $\sim 10^{\pm 1}$ for the other combinations (n_0, T_{CS}) and (n_{CS}, T_0)].

In the simulation, the time interval between main peaks of the reconnection rate is of order $t_R \sim 200 \tau_A$, which is about $\sim 13 \delta_x/V_A$ (Alfvén crossing times based on the average distance ($\delta_x \approx 15 l_{CS}$) between neighbouring X points). We now scale the timescale $t_R \sim 13 \delta_x/V_A$ to the much larger distances expected in the corona, using $\delta_x \sim \lambda_{mfp}$ (which implies $t_R \propto n_0^{-1/2} T_0^2 B_0^{-1}$). For $B_0 = 70$ G and three different values of the density, we derive the timescale t_R in the range of temperatures $T = (2.5-9) \times 10^6$ K. This yields $t_R = 1-13$ s for $n = 10^9$ cm $^{-3}$; $t_R = 0.7-8$ s for $n = 3 \times 10^9$ cm $^{-3}$; and $t_R = 0.4-4$ s for $n = 10^{10}$ cm $^{-3}$. Since the elongation and structuring of the area of anomalous resistivity (which is the dominant factor controlling the dynamics) takes place in the inflow sections of the current sheet, where the density and temperature are close to the external values n_0 and T_0 , the estimate $t_R \sim 1$ s may be the most realistic one. In view of the uncertainties of the parameter determinations, this is amazingly close to the observed intervals between the radio pulses, $t_{radio} \approx 0.5-3$ s.

The Poynting flux of electromagnetic energy toward the current sheet is $\mathcal{P}_{in} = 2(B_0^2/\mu_0)\bar{u}_{in}L_{CS}L_z$, where L_{CS} is the vertical (x -) extent of the current sheet and the average inflow velocity can be expressed using the average reconnection rate \bar{R} as $\bar{u}_{in} \sim \bar{R}V_A$. Using $L_{CS} \sim L_z \sim 10^9$ cm and $\bar{R} \sim 0.02$ (from Fig. 8), we find $\mathcal{P}_{in} \sim 8 \times 10^{27}$ erg s $^{-1}$. This appears to be a reasonable value, since it exceeds the increase rate of the thermal energy in the flare loop obtained by Ohyama & Shibata (1998) by a moderate factor (~ 3) consistent with the fact that not all of the inflowing electromagnetic energy can be dissipated. The scaling $\mathcal{P}_{in} \propto B_0^3 n_0^{-1/2}$ shows that higher energy inflow rates can easily be achieved by modest increases of B_0 .

On the other hand, the rate of particles flowing into the current sheet, $\dot{N} = 2n_0\bar{u}_{in}L_{CS}L_z$, seems to fall short of the requirement on the acceleration rate of HXR-emitting particles, which is on the order of $\sim 10^{35}-10^{36}$ s $^{-1}$ for an M class flare. Our parameters n_0, B_0 yield $\dot{N} \sim 2 \times 10^{34}$ s $^{-1}$, and the number of particles that can be accelerated out of this population must be significantly smaller. The scaling $\dot{N} \propto B_0 n_0^{1/2}$ shows that this dilemma cannot be overcome without supposing very high values of n_0 and B_0 (and T_0 — to keep $t_R \sim 1$ s) and, hence, increasing \mathcal{P}_{in} by a huge amount. Even an increase of the average reconnection rate by one order of magnitude could only weaken but not eliminate the problem. Whereas a sufficient number of particles is available within the current sheet to account for the decimetric radio source, it is likely that acceleration

in additional volumes contributes significantly to the flux of HXR-emitting particles. Possibilities for this are (1) the spreading of the acceleration volume by waves which accelerate particles stochastically (e.g., Miller et al. 1996), or (2) the interaction between the reconnection outflow and the low-lying loop, where the density is higher (Tsuneta 1995), or (3) the transmission of magnetic stresses, which are created in the current sheet by reconnection, along the field lines to a more dense acceleration region near the base of the corona (Haerendel 1994). The detailed correlation at small timescales between the HXR and the decimetric emissions will then be relatively weak, at least for possibilities (2) and (3), — as is observed in the October 5, 1992 flare and in many other events (Aschwanden et al. 1990).

Maximum energies of particles accelerated by the DC electric field near X points have been found to reach $W_{\max} \sim (m_e/m_i)^{1/4} e \delta_x E$ (in the ideal case of test particle behaviour with no back-reaction on the electromagnetic fields) (Kliem 1994; Kliem et al. 1998). This falls into the MeV range for all values of n , T , and B considered here. Thus, energies of radio-emitting particles in flares (~ 25 – 100 keV) can be reached easily.

3.5. Plasmoid evolution and frequency drift of the radio emission

The centre frequency of the decimetric continuum and pulses was drifting on average toward lower frequencies during the whole event. This implies in our model that the plasmoid was not stationary but moving upwards during the whole radio burst so that the expansion at greater heights could counteract the density increase due to reconnection (Fig. 9). If we extrapolate the observed height-time plot of the plasmoid (Fig. 3 in Ohyama & Shibata 1998) backwards, based on the assumption of constant acceleration from zero velocity at $t_0 = 9:23:20$ UT to the observed velocity at 9:25 UT, we arrive at a starting point, $h(t_0) \sim 1.3 \times 10^4$ km, high above the top of the flare loop [$h_{\text{fl}}(t < 9:24:20 \text{ UT}) \lesssim 3 \times 10^3$ km], which is consistent with our simplified 2D model.

Since $\beta \ll 1$ in the corona, the magnetic forces dominate the acceleration of plasmoids. In our model of plasmoid formation in a preexisting current sheet, this implies that the reconnection rate at the X point below the plasmoid exceeded the reconnection rate at the X point above the plasmoid. The imbalance of the reconnected flux then led to the upward bulk acceleration of the plasmoid.

It has been found in previous non-symmetric simulations of dynamic current sheet evolution (using a smaller box and partly different initial conditions; Schumacher & Kliem 1996) that the reconnection rate is most strongly enhanced during the buildup phase of a strong asymmetry, while the bulk velocity of the plasmoid reaches its peak value somewhat later (by $\sim 50 \tau_A$ in those simulations). It is thus expected that the most prominent temporary

increases of the reconnection rate are associated with (1) enhanced particle acceleration, corresponding to enhanced radio and X-ray flux, (2) an initial rise of pressure and density in the plasmoid from the enhanced reconnection outflow into the plasmoid, corresponding to a rise of the frequency of plasma emission, and (3) the buildup of a strong asymmetry of the reconnected flux and, hence, a strong acceleration of the plasmoid, corresponding to a strong negative drift of the radio emission frequency in the inhomogeneous solar atmosphere, following the initial rise of the emission frequency. The radio and hard X-ray data suggest such an association during the intervals of strong flux rise (near 9:24:30, 9:24:45, and 9:25:50 UT). The same effect is indicated also at the beginning of the event (near 9:23:30 UT).

The interplay between the increase of the density in the plasmoid by reconnection and the decrease by upward motion and expansion can lead to a constant or even decreasing frequency drift rate of the radio emission — in spite of increasing plasmoid velocity. Also the soft X-ray observations suggest that the density of the plasmoid was only weakly decreasing during its rise from 2.5×10^4 km at 9:25 UT to 5.2×10^4 km at 9:26 UT. Ohyama & Shibata (1998) derived densities $n_{\text{pl}} \sim (0.8\text{--}1.6) \times 10^{10} \text{ cm}^{-3}$ and $n_{\text{pl}} \sim (0.6\text{--}1) \times 10^{10} \text{ cm}^{-3}$, respectively, at these two instants (cf. their Tables 1 and 3).

The very high frequency drift rates of the individual pulses were not measured. An earlier statistical investigation of individual pulse drifts at decimetric frequencies in 10 pulsation events has shown a narrow distribution peaking at $df/dt \approx 3 \text{ GHz s}^{-1}$, consistent with compact sources of enhanced density and a scale height of $\sim (2\text{--}20) \times 10^3$ km (Aschwanden & Benz 1986). We note that the plasmoid observations during the October 5, 1992 flare as well as our model are fully consistent with those source characteristics. The weak statistical tendency of individual pulses toward positive frequency drift is consistent with the density increase of the plasmoid associated with each single coalescence event.

Although the dynamical behaviour of the pulsating decimetric radio burst, as well as the majority of the hard and soft X-ray data, appear to be consistent with our model of the formation and acceleration of a (single) large-scale plasmoid by dynamic magnetic reconnection, more complex scenarios are not excluded. For example, it is possible that the pulsating radio emission before 9:24:20 UT belonged to a separate plasmoid, which may have formed independently if the current sheet had a large extent along the line of sight (z direction in the simulation). The drop of the radio flux around 9:24:10 UT may perhaps be explained by such a multiple source structure. Also the existence of two additional weak emission bands, which showed signs of pulsations not or only weakly correlated with the pulses of the main radio source (Fig. 4), suggests the formation of two additional radio sources (plas-

moids separated from the main plasmoid in the x or z direction, which are not resolved in the soft X-ray images).

The variations of the frequency drift rate may have been influenced also by acceleration or deceleration of the plasmoid by the expanding loop, if it was in fact connected with the plasmoid.

4. Discussion

The aspect ratio $r_\eta = \delta x_\eta / \delta y_\eta$ reaches $\sim 10^2$ in the simulation. The estimates of Sect. 3.4 suggest that $r_\eta \gtrsim 10^3$ in the corona. This suggests that the modulations of the reconnection rate, $R(t)$, become even deeper than in the simulation, since R is reduced more strongly during the phases of Sweet-Parker reconnection. This is in favour of deep modulations of the particle acceleration rate like that observed in the flare under study.

Anomalous resistivity is created by kinetic current-driven instabilities, which have the ion cyclotron radius, r_{ci} , and the ion inertial length, d_i , as natural scales. For our external plasma parameters B_0 , n_0 , and T_0 , for example, we have $r_{ci} \sim 20$ cm and $d_i \sim 700$ cm. Thus, it is probable that the kinetic processes lead to small-scale ($L \ll \lambda_{mfp}$) and short-lived ($\tau \ll t_R$) inhomogeneities of the anomalous resistivity. This may enforce intermittent excitation of small-scale magnetic islands. Such small-scale structures may be destroyed again by diffusion or may merge into larger islands and enter finally into the coalescence and plasmoid formation process on scales at which a fluid description is appropriate.

More complicated schemes of dynamic reconnection are conceivable, based on quasi-periodicities in complex multiple island coalescence processes (Kliem 1988). In that paper it was suggested that new islands are not formed as single entities, but that excitation of the tearing mode in the elongated flat sections of the current sheet creates a chain of islands. The subsequent evolution may be rather similar to the dynamics obtained here. Since the initial phase of the coalescence instability is an ideal MHD process, this instability develops faster than the tearing instability. Therefore, in the presence of perturbations, it takes over as the nonlinear evolution of the tearing instability (inhibiting saturation of the tearing instability to a regular chain of islands). The multiple coalescence of the island chain in a section of the current sheet leads to formation and amplification of plasmoids, similar to the evolution found here; it may even be more dynamic. Cyclic repetition of the sequence of tearing instability, coalescence instability, and re-creation of long, flat current sheet sections between plasmoids may result in pulsed particle acceleration and radio emission. Some aspects of such a complex reconnection process have been studied by Schumacher & Kliem (1996, 1997).

Also externally triggered magnetic reconnection can show secondary tearing. This was found by Odstrčil &

Karlický (1997) for the case of triggering by a weak shock wave incident on a current sheet.

Alternatively, or in addition to variable particle acceleration, the pulses of the radio flux may be caused by varying efficiency of the emission process in the disturbed and highly inhomogeneous plasma of the dynamic current sheet. For example, the irregular oscillations of the central plasmoid, which were mentioned in Sect. 3.2 and are indicated by the variations of its peak pressure in Fig. 9, could influence the radio emissivity. However, varying particle acceleration is a natural and immediate consequence of dynamic reconnection. A quantitative investigation of varying emission efficiency is made difficult by insufficient knowledge of the distribution function of the energetic particles and, hence, of the kinetic plasma physics of the emission process.

An interpretation of the weak anticorrelation between the decimetric pulses and the HXR lightcurve at short timescales (Fig. 5) in terms of our current sheet model is possible but remains speculative. A tentative interpretation may be based on the oscillations of the central plasmoid: The outflow of plasma and accelerated particles from the main X points into the plasmoid is hampered, while the outflow away from the plasmoid is supported, during phases of plasmoid expansion in the x direction; and the situation is reversed during plasmoid expansion in the y direction. Alternatively, the anticorrelation could, for example, be related to disturbances of the radio source caused by temporarily enhanced particle acceleration in other parts of the active region (cf. Sect. 3.4). Studies of a larger sample of events will be required to confirm the anticorrelation as a general property and to determine possible causes.

A model in which the pulsating radio burst is associated with a plasmoid implies a strong role of trapping of downward propagating particles in the cusp between the current sheet and the underlying flare loop. The weakness of pulsations in the HXR burst is thus naturally explained. This would be difficult if the radio source were formed within the flare loop, as is commonly supposed for decimetric continuum bursts and was assumed for the October 5, 1992 event by Aschwanden & Benz (1995).

An association of radio continuum burst sources with plasmoid ejections had previously been found in case of isolated sources of moving type IV bursts at metric and decametric frequencies and much larger heights in the corona ($\gtrsim 2 \times 10^{10}$ cm; e.g., Gopalswamy et al. 1997). Recently, also Hori (1999) suggested an association between drifting decimetric/metric continuum bursts and the ejection of plasmoids for the flares of October 5, 1992 and June 28, 1993.

The proposed mechanism of variable particle acceleration may also underlie quasi-periodic sequences of type III bursts (Aschwanden et al. 1994). These events are also associated with the impulsive phase of solar flares and their timescales are similar to those of the pulsations consid-

ered here ($\sim 0.5\text{--}5$ s). A stronger role of particle escape and a weaker influence of particle trapping may lead to chains of type III bursts instead of a pulsating radio continuum. This appears possible in case of strongly asymmetric reconnection, where the field lines passing through the vicinity of the strongest X point below the plasmoid do not immediately close at the X point above the plasmoid, or in case of a sufficiently strong guide field component, $B_z > B_{x0}$, where the particles can easily escape from the plasmoid into the z direction. Since type III burst sources generally follow open field lines, the current sheet should extend into interplanetary space, i.e., exist prior to the flare event in those cases.

5. Conclusions

(1) We have presented a new model of pulsating radio bursts, in which the variations of the flux are caused by modulations of the particle acceleration in a highly dynamic reconnection process. This process operates in extended coronal current sheets and includes (in a fluid model) the self-consistent evolution of anomalous resistivity. It involves the repeated formation of magnetic islands, their coalescence, and the formation of one (or several) dense and hot plasmoid(s) which can finally be ejected. This model is able to explain the occurrence of irregular or quasi-periodic pulses with timescales in the range $\sim 0.5\text{--}10$ s. It is also consistent with the usually low amplitude of modulation of the hard X-ray emission and with the observed weak anticorrelation between the hard X-ray and decimetric emissions at short timescales in the flare of October 5, 1992 considered here.

(2) The unified explanation of plasmoid formation and pulsating radio emission supports the conclusion by Ohya & Shibata (1998) that the current sheet in the considered flare was not formed by the ejection of the plasmoid (contrary to the often favoured view of eruptive flare processes). The model is consistent with both of the two remaining possibilities — formation and acceleration of the plasmoid within a preexisting current sheet or simultaneous formation of both structures by a global MHD instability.

(3) The emission mechanism of the radio waves may differ from the standard model of radio continuum bursts in the decimetric and metric range, which supposes particle injection and trapping in a stable coronal loop and subsequent evolution of a loss-cone particle distribution. Instead, a large fraction of the accelerated particles may only temporarily be trapped in the plasmoid, and the acceleration process itself may form an anisotropic velocity distribution, which is unstable against electrostatic or electromagnetic wave excitation.

(4) We have confirmed and extended previous numerical studies of impulsive bursty reconnection, in particular the finding that magnetic reconnection, which is triggered by anomalous resistivity, proceeds in a highly vari-

able manner if long current sheets are considered and the temporal and spatial evolution of the anomalous resistivity is self-consistently taken into account.

Acknowledgements. We gratefully acknowledge the very helpful comments by K.-L. Klein and the anonymous referee. The Zürich radio observations are partially financed by SNF grant 20-53664.98. Technical support regarding the presentation of the Ondřejov radio data was given by H. Mészárosóvá. This work was supported by DLR grant 50OC9706 and by the key projects K1-003-601 and K1-043-601, and the grant A3003707 of the Academy of Sciences of the Czech Republic. The John von Neumann-Institut für Computing, Jülich granted Cray computer time.

References

- Ambrosiano J., Matthaeus W.H., Goldstein M.L., Plante D., 1988, *J. Geophys. Res.* 93, 14 383
- Aschwanden M.J., 1987, *Solar Phys.* 111, 113
- Aschwanden M.J., Benz A.O., 1986, *A&A* 158, 102
- Aschwanden M.J., Benz A.O., 1995, *ApJ* 438, 997
- Aschwanden M.J., Benz A.O., Kane S.R., 1990, *A&A* 229, 206
- Aschwanden M.J., Benz A.O., Schwartz R.A., 1993, *ApJ* 417, 790
- Aschwanden M.J., Benz A.O., Montello M.L., 1994, *ApJ* 431, 432
- Aschwanden M.J., Bynum R.M., Kosugi T., Hudson H.S., Schwartz R.A., 1997, *ApJ* 487, 936
- Aschwanden M.J., Kliem B., Schwarz U., Kurths J., Dennis B.R., Schwartz R.A., 1998, *ApJ* 505, 941
- Bastian T.S., Benz A.O., Gary D.E., 1998, *ARA&A* 36, 131
- Birn J., Thomsen M.F., Borovsky J.E., et al., 1998, *J. Geophys. Res.* 103, 9235
- Biskamp D., 1982, *Z. Naturforsch.* 37a, 840
- Biskamp D., 1986, *Phys. Fluids* 29, 1520
- Biskamp D., 1994, *Phys. Reports* 237, 179
- Deeg H.-J., Borovsky J.E., Duric N., 1991, *Phys. Fluids B* 3, 2660
- Forbes T.G., Priest E.R., 1987, *Rev. Geophys.* 25, 1583
- Gopalswamy N., Kundu M.R., Manoharan P.K., et al., 1997, *ApJ* 486, 1036
- Haerendel G., 1994, *ApJS* 90, 765
- Hori K., 1999, In: *Solar Physics with Radio Observations*, Bastian T., Gopalswamy N., Shibasaki K. (eds.), Nobeyama Radio Observatory, NRO Report No. 479, p. 267
- Karlický M., 1988, *Bull. Astron. Czech.* 39, 13
- Karpen J.T., Antiochos S.K., DeVore C.R., 1995, *ApJ* 450, 422
- Kiplinger A.L., Dennis B.R., Frost K.J., Orwig L.E., Emslie A.G., 1983, *ApJ* 265, L99
- Kliem B., 1988, *ESA SP-285*, Vol. 2, 117
- Kliem B., 1994, *ApJS* 90, 719
- Kliem B., Schumacher J., 1996, In: *Magnetodynamic Phenomena in the Solar Atmosphere — Prototypes of Stellar Magnetic Activity*, Uchida Y., Kosugi T., Hudson H.S. (eds.), Kluwer, Dordrecht, p. 305
- Kliem B., Schumacher J., Shklyar D.R., 1998, *Adv. Space Res.* 21(4), 563
- Krüger A., 1979, *Introduction to Solar Radio Astronomy and Radio Physics*, D.Reidel Publ. Comp., Dordrecht

- Kuijpers J., 1980, In: Radio Physics of the Sun, Kundu M.R., Gergely T.E. (eds.), IAU Symp. 86, Reidel, Dordrecht, p. 341
- Kulsrud R.M., 1998, Phys. Plasmas 5, 1599
- Magara T., Shibata K., Yokoyama T., 1997, ApJ 487, 437
- Masuda S., Kosugi T., Hara H., Tsuneta S., Ogawara Y., 1994, Nature 371, 495
- Miller J.A., LaRosa T.N., Moore R.L., 1996, ApJ 461, 445
- Moses R.W., Finn J.M., Ling K.M., 1993, J. Geophys. Res. 98, 4013
- Odr  il D., Karlick   M., 1997, A&A 326, 1252
- Ohyama M., Shibata K., 1998, ApJ 499, 934
- Papadopoulos K., 1979, In: Dynamics of the Magnetosphere, Akasofu S.-I. (ed.), Reidel, Dordrecht, p. 289
- Priest E.R., 1982, Solar Magnetohydrodynamics, D.Reidel Publ. Comp., Dordrecht
- Priest E.R., 1985, Rep. Prog. Phys. 48, 955
- Priest E.R., Forbes T.G., 1986, J. Geophys. Res. 91, 5579
- Sato J., Sawa M., Masuda S., et al., 1998, The Yohkoh HXT Image Catalogue, October 1991–August 1998, Nobeyama Radio Observatory, Nobeyama
- Sato T., Hayashi T., 1979, Phys. Fluids 22, 1189
- Scholer M., 1991, Geophys. Astrophys. Fluid Dyn. 62, 51
- Scholer M., Jamitzky F., 1987, J. Geophys. Res. 92, 12 181
- Scholer M., Roth D., 1987, J. Geophys. Res. 92, 3223
- Schumacher J., Kliem B., 1996, Phys. Plasmas 3, 4703
- Schumacher J., Kliem B., 1997, Phys. Plasmas 4, 3533
- Schumacher J., Kliem B., Seehafer N., 2000, Phys. Plasmas 7, 108
- Tsuneta S., 1995, Publ. Astron. Soc. Japan 47, 691
- Tsuneta S., 1996, ApJ 456, 840 (erratum: ApJ 464, 1055)
- Tsuneta S., 1997, ApJ 483, 507
- Ugai M., 1992, Phys. Fluids B 4, 2953
- Ugai M., 1993, Phys. Fluids B 5, 3021
- Ugai M., 1995, Phys. Plasmas 2, 388
- Ugai M., Tsuda T., 1977, J. Plasma Phys. 17, 337
- Yokoyama T., Shibata K., 1994, ApJ 436, L197